

# Carbon storage in Earth's deep interior implied by carbonate-silicate-iron melt miscibility

Anne H. Davis<sup>1</sup>, Natalia Viatcheslavovna Solomatova<sup>2</sup>, Razvan Caracas<sup>3</sup>, and Andrew J. Campbell<sup>4</sup>

<sup>1</sup>University of Oslo

<sup>2</sup>CNRS, ENS de Lyon

<sup>3</sup>French National Centre for Scientific Research (CNRS)

<sup>4</sup>University of Chicago

February 13, 2023

## Abstract

Carbonate melts have been proposed to exist in the lower mantle, but their interaction with other lower mantle melt compositions is poorly understood. To understand miscibility in the carbonate-silicate-metal melt system, we simulate endmember, binary, and ternary melt mixtures and study how their Gibbs free energies of mixing evolve with pressure. We find that carbonate-metal and carbonate-silicate melts have miscibility gaps that close with increasing pressure, while silicate-metal melts are immiscible at all lower-mantle pressures. Extending this analysis to the core-mantle boundary, we suggest three miscible melt fields near the endmember carbonate, silicate, and iron melt compositions. Analysis of the densities of these miscible melt compositions indicates that some carbonate-rich and some silicate-rich melt compositions are gravitationally stable at the core-mantle boundary and could be candidate compositions to explain ultra-low velocity zones. Additionally, we evaluate the speciation of an example immiscible melt composition at various pressures throughout the mantle and identify reduced carbon species that would be expected to form in the melt. Our analysis reveals that a majority of Earth's carbon could have been transported to the core during core-mantle differentiation and that much of Earth's carbon may be stored in the deep interior today.

## Hosted file

955318\_0\_art\_file\_10675923\_rpx4ht.docx available at <https://authorea.com/users/582798/articles/622731-carbon-storage-in-earth-s-deep-interior-implied-by-carbonate-silicate-iron-melt-miscibility>

## Hosted file

955318\_0\_supp\_10669123\_rpjlsj.docx available at <https://authorea.com/users/582798/articles/622731-carbon-storage-in-earth-s-deep-interior-implied-by-carbonate-silicate-iron-melt-miscibility>

1  
2 **Carbon storage in Earth's deep interior implied by carbonate-silicate-iron melt**  
3 **miscibility**

4 **A.H. Davis<sup>1,\*</sup>, N.V. Solomatova<sup>2</sup>, R. Caracas<sup>3,4</sup>, and A.J. Campbell<sup>1</sup>**

5 <sup>1</sup>Department of the Geophysical Sciences, University of Chicago, Chicago, IL, USA.

6 <sup>2</sup>Terramera, Vancouver, British Columbia, Canada. <sup>3</sup>The Center for Earth Evolution and

7 Dynamics (CEED), University of Oslo, Oslo, Norway. <sup>4</sup>Université de Paris, Institut de Physique

8 du Globe de Paris, CNRS, Paris, France. \*Now at CEED, University of Oslo, Oslo, Norway.

9 Corresponding author: Anne Davis ([a.h.davis@geo.uio.no](mailto:a.h.davis@geo.uio.no))

10 **Key Points:**

- 11 • Carbonate-iron and carbonate-silicate melts have miscibility gaps that close with  
12 increasing pressure.
- 13 • Carbonate-silicate-iron melts may contribute to the existence of ultra-low velocity zones  
14 at the core-mantle boundary.
- 15 • Carbon's affinity for iron indicates that much of Earth's carbon could have been  
16 transported to the core during core-mantle differentiation.  
17

## 18 **Abstract**

19 Carbonate melts have been proposed to exist in the lower mantle, but their interaction  
20 with other lower mantle melt compositions is poorly understood. To understand miscibility in the  
21 carbonate-silicate-metal melt system, we simulate endmember, binary, and ternary melt mixtures  
22 and study how their Gibbs free energies of mixing evolve with pressure. We find that carbonate-  
23 metal and carbonate-silicate melts have miscibility gaps that close with increasing pressure,  
24 while silicate-metal melts are immiscible at all lower-mantle pressures. Extending this analysis  
25 to the core-mantle boundary, we suggest three miscible melt fields near the endmember  
26 carbonate, silicate, and iron melt compositions. Analysis of the densities of these miscible melt  
27 compositions indicates that some carbonate-rich and some silicate-rich melt compositions are  
28 gravitationally stable at the core-mantle boundary and could be candidate compositions to  
29 explain ultra-low velocity zones. Additionally, we evaluate the speciation of an example  
30 immiscible melt composition at various pressures throughout the mantle and identify reduced  
31 carbon species that would be expected to form in the melt. Our analysis reveals that a majority of  
32 Earth's carbon could have been transported to the core during core-mantle differentiation and  
33 that much of Earth's carbon may be stored in the deep interior today.

## 34 **Plain Language Summary**

35 Understanding the storage and cycling of carbon in the Earth's deep interior improves our  
36 knowledge of the Earth's formation and evolution throughout geologic time. Carbon-bearing  
37 melts are candidate phases for carbon storage in the lower mantle and may react and mix with  
38 other melt phases at places like the core-mantle boundary. The extent of mixing upon reaction is  
39 dependent on the thermodynamic properties of the mixture components and determines the  
40 possible range of compositions, structures, and densities of multicomponent melt mixtures. To  
41 determine possible melt compositions that may arise from mixtures of carbonate, silicate, and  
42 iron melts in the lower mantle and their physical and chemical properties, we performed  
43 molecular simulations to determine whether a mixture will separate or stay mixed. We find that  
44 carbonate melts mix with silicate and iron melts at all lower mantle pressures, and that mixing in  
45 the carbonate-silicate-iron melt system increases with pressure. Additionally, we find that certain  
46 melt mixtures have densities at the core-mantle boundary that make them candidate compositions  
47 to explain ultra-low velocity zones. Finally, we find that carbon has an affinity for iron that leads  
48 to the formation of carbide-like structures that may have allowed carbon to become sequestered  
49 in the Earth's core during core formation.

## 50 **1 Introduction**

51 Carbon plays a vital role at Earth's surface in biological and atmospheric processes, but  
52 the role of carbon in the deep Earth is less well understood. Carbon and other volatiles in the  
53 lower mantle are thought to be remnants of an early magma ocean (Labrosse et al., 2007) or to  
54 derive from subducting slabs (Plank & Manning, 2019). However, reports vary on the carbon  
55 content of the Earth (Javoy, 1997; McDonough & Sun, 1995), the distribution of carbon between  
56 core and mantle (Dasgupta & Walker, 2008; Wood et al., 2013), the phase relations of carbon-  
57 bearing phases at depth (Merlini et al., 2012; Oganov et al., 2008), and the reactivity of carbon-  
58 bearing phases with the surrounding core and mantle. The existence and role of carbonates in the  
59 lower mantle is highly contested. Multiple studies show that carbonates undergo melting (Li et  
60 al., 2017), reduce to diamond or iron carbide (Rohrbach & Schmidt, 2011), or decarbonate  
61 (Drewitt et al., 2019) before they reach the lower mantle in subducting slabs. However, the

62 stability of carbonate phases depends on a host of thermodynamic variables, including pressure,  
63 temperature, and oxygen fugacity. Reports of carbonate melt inclusions in deep Earth diamonds  
64 (Korsakov & Hermann, 2006) as well as petrologic experiments on solid carbonates in lower  
65 mantle phase assemblages (Dorfman et al., 2018; Lv et al., 2021) indicate that carbonates and  
66 carbonate melts may be stable and present in the lower mantle, plausibly even in the core-mantle  
67 boundary region. However, few studies have examined carbonate melt interactions in the lower  
68 mantle.

69 Previous *ab initio* studies have examined carbonate melts (Koura et al., 1996; Li et al.,  
70 2017; Xu et al., 2020), carbon-bearing silicate melts (Bajgain & Mookherjee, 2021; Ghosh et al.,  
71 2017; Ghosh & Karki, 2017), carbon and iron-bearing silicate melts (Karki et al., 2020;  
72 Solomatova & Caracas, 2021; Solomatova et al., 2019, 2020), and carbon partitioning between  
73 silicate and iron melts (Zhang & Yin, 2012). This work and Davis et al. (2022) represent the first  
74 *ab initio* studies with subequal amounts of carbon, silicon, and metal in a melt composition. In  
75 this study, we simulate seven total endmember, binary, and ternary melt compositions (Table 1)  
76 at pressures between 0-200 GPa and at a temperature of 4,000 K to estimate melt miscibility,  
77 structure, and density. With these results, we determine the degree of mixing in the carbonate-  
78 silicate-iron ternary system, the buoyancies of the melts that form, and the chemical species that  
79 exist within the melt. We evaluate the viability of carbonate-silicate-metal melt compositions as  
80 contributors to ultra-low velocity zones (ULVZs) and the implications for carbon sequestration  
81 and distribution throughout Earth's mantle and core.

## 82 **2 Methods**

83 *Ab initio* molecular dynamics simulations using the projector-augmented wave method  
84 (Kresse & Furthmuller, 1996) of density functional theory were performed with the Vienna *ab*  
85 *initio* simulation package (Blochl, 1994). We used the generalized gradient approximation in the  
86 Perdew-Burke-Ernzerhof form (Perdew et al., 1996) to treat electron exchange and correlation.  
87 The kinetic energy cutoffs for the plane-wave expansion of the wavefunctions were set to 600  
88 eV. We used the canonical ensemble (NVT) with a Nosé-Hoover thermostat (Hoover, 1985;  
89 Nosé, 1984) with a time step of 1-2 fs for 18-80 ps, depending on the density. The Brillouin zone  
90 was sampled at the gamma point. The calculations were spin-polarized at all pressures. A  
91 Hubbard  $U_{eff}$  (U-J) parameter of 4 eV was applied, which enhances the magnetic moment of the  
92 Fe atoms and corrects for their volume and coordination environment. The mean-square  
93 displacement as a function of time shows a ballistic regime below approximately 1,000 fs, after  
94 which the atoms reach a diffusive regime. For the carbonate-silicate-metal melt composition,  
95 calculations were run with a minimum of two starting configurations, and results were averaged.  
96 We employ the Universal Molecular Dynamics (UMD) package for the analysis of the results  
97 (Caracas et al., 2021).

98 We work with seven melts representing endmember ( $MgCO_3$ ,  $MgSiO_3$ , and Fe), binary  
99 ( $Mg(C,Si)O_3$ ,  $MgCO_3 + Fe$ ,  $MgSiO_3 + Fe$ ), and ternary ( $Mg(C,Si)O_3 + Fe$ ) melt compositions  
100 (Table 1), with supercells ranging from 108-133 atoms. Simulations span a pressure range of 0-  
101 200 GPa, and all calculations are performed at 4,000 K. Bond distances were determined from  
102 the pair distribution functions. The first peak in the pair distribution function marks the radius of  
103 the first coordination sphere for the reference atom, and the first minimum translates to the  
104 maximum acceptable bond distance for a bonding pair. The fitted minimum values were used in  
105 the speciation analysis to determine carbon clusters.

Table 1  
*Melt Compositions Simulated*

Melt	Mg	Si	C	O	Fe	Total
MgCO <sub>3</sub>	24	0	24	72	0	120
MgSiO <sub>3</sub>	24	24	0	72	0	120
Fe	0	0	0	0	108	108
Mg(C,Si)O <sub>3</sub>	24	12	12	72	0	120
MgCO <sub>3</sub> + Fe	24	0	24	72	13	133
MgSiO <sub>3</sub> + Fe	24	24	0	72	13	133
Mg(C,Si)O <sub>3</sub> + Fe	24	12	12	72	13	133

*Note.* The numbers refer to the number of atoms included in the simulation.

### 106 3 Melt miscibilities

107 The Gibbs free energy of mixing,  $\Delta G_{\text{mix}}$ , determines whether a given solution of melt  
 108 components will mix or unmix. Negative  $\Delta G_{\text{mix}}$  values indicate a mixture is energetically  
 109 favorable and therefore miscible. Positive  $\Delta G_{\text{mix}}$  values indicate a mixture is energetically  
 110 unfavorable and therefore immiscible. The Gibbs free energy of mixing was estimated using the  
 111 following equation:

$$112 \quad \Delta G_{\text{mix}} = \Delta H_{\text{mix}} - T\Delta S_{\text{mix}} + \int P\Delta V_{\text{mix}} \quad (1)$$

113 where  $\Delta H_{\text{mix}}$  is the enthalpy of mixing, T is the temperature,  $\Delta S_{\text{mix}}$  is the entropy of mixing, P is  
 114 the pressure, and  $\Delta V_{\text{mix}}$  is the mixing volume. An example of the contribution of each term to  
 115  $\Delta G_{\text{mix}}$  on the carbonate-silicate binary is shown in Figure S1. We describe the calculation of each  
 116 term in the equation in the following sections.

#### 117 3.1 Enthalpy of mixing

118 To calculate the enthalpy of mixing, we use the equation:

$$119 \quad \Delta H_{\text{mix}} = \sum_{i \neq j} \beta_{ij} X_i X_j \quad (2)$$

120 where  $\beta_{ij}$  represents the binary parameter along the i-j binary, and  $X_i$  and  $X_j$  represent the mole  
 121 fractions of the i and j components, respectively. To find appropriate values for  $\beta$ , we plot  $\Delta G_{\text{mix}}$   
 122 at 0 GPa along a binary and select  $\beta$  values that match the expected degree of mixing in each  
 123 binary system (Figure S2). Reasonable degrees of mixing are determined from examining  
 124 solubility experiments on binary systems in addition to our own simulation results at 0 GPa. A  
 125 study of orthopyroxene solubility in carbonate melts reports that carbonate melts contain 4  
 126 atomic percent silicate at 2 GPa and 1273 K (Kamenetsky & Yaxley, 2015). We select a value of  
 127 95 kJ for  $\beta$  on the carbonate-silicate join, which leads to silicate solubility of 8 atomic percent in  
 128 carbonate melts at 4,000 K. Silicate-metal melts are immiscible at 0 GPa (Fichtner et al., 2021),  
 129 and our simulations show groupings of silicon and iron atoms that is suggestive of immiscibility.  
 130 Thus, we select a  $\beta$  parameter of 135 kJ, which leads to limited miscibility (2 atomic percent Fe  
 131 in silicate melt) at 0 GPa and 4,000 K. Experimental reports of carbonate solubility in iron melt  
 132 are lacking, but our carbonate-metal simulation indicates less miscibility than the carbonate-  
 133 silicate simulation and more miscibility than the silicate-metal simulation at 0 GPa. We select a  
 134 value of 115 kJ for the  $\beta$  parameter, which leads to 4 atomic percent Fe in carbonate melt.

## 135 3.2 Entropy of mixing

136 To calculate the entropy of mixing, we use the ideal entropy of mixing:

137 
$$\Delta S_{mix} = -R(X_i \ln X_i + X_j \ln X_j + X_k \ln X_k) \quad (3)$$

138 where R is the gas constant and  $X_i$ ,  $X_j$ , and  $X_k$  are the mole fractions of the i, j, and k  
139 components, respectively.

## 140 3.3 Mixing volumes

141 Mixing volumes are calculated by taking weighted averages of molar volumes of  
142 individual melt components. To calculate molar volumes, we first fit either second or third order  
143 Birch-Murnaghan equations of state for our simulated melt compositions (Figure 1a). We also  
144 include the pyrolite and pyrolite+8CO compositions from Solomatova et al. (2019) for  
145 comparison. Equation of state fit parameters are reported in Table S8. The fit parameters reveal  
146 that melts with a carbonate component are highly compressible, which is in agreement with  
147 previous studies of carbon-bearing melts (Ghosh & Karki, 2017; Ghosh et al., 2007; Sakamaki et  
148 al., 2011). There is significant covariance between  $K_0'$ ,  $K_0$ , and  $V_0$  values for all melts, which is  
149 common in finite strain equations of state. One continuous equation of state was fit across  
150 multiple structural transitions, which stem from gradual coordination changes in the melt.  
151 However, the majority of coordination changes occur between 0 and 20 GPa, below the pressure  
152 regime of interest. In the pressure regime of the lower mantle, the fits closely match the data.  
153 Using the Birch-Murnaghan equation of state fits, we calculate molar volumes of the melts at  
154 pressures from 0 to 200 GPa (Figure 1b). Due to the non-stoichiometric nature of the melt  
155 mixtures, we calculate volumes per mole of atoms instead of per formula unit, allowing the  
156 molar volumes to be directly compared. Iron and iron-bearing melts have the largest molar  
157 volumes, while pyrolite melts have the smallest. The densities and molar volumes of each melt  
158 composition are reported in Tables S1-S7.

159 To calculate the mixing volumes, we compare the molar volume of our simulated mixture  
160 with the weighted average of the molar volumes of the mixture components. The magnitude of  
161 the mixing volume indicates the nonideality of a melt mixture and the degree of interaction  
162 between melt components. As the pressure derivative of  $\Delta G_{mix}$ , the mixing volume is the  
163 tendency of a mixture to become more or less energetically favorable with changing pressure.  
164 Thus, the sign of the mixing volume is suggestive of miscibility in multicomponent mixtures.  
165 This is especially true at high pressures, where the mixing volume term dominates the  
166 contribution to  $\Delta G_{mix}$ . For instance, a composition that is 50%  $MgSiO_3$  and 50% Fe has a  $\Delta G_{mix}$   
167 value of 58 kJ at 136 GPa and 4,000 K (see Figure 3). Of the 58 kJ, 47 kJ is from the mixing  
168 volume component, accounting for 82% of the contribution to  $\Delta G_{mix}$ . Mixtures with positive  
169 mixing volumes become larger upon mixing and become less stable with increasing pressure,  
170 enforcing immiscibility. The mixing volumes for the four multicomponent melts in this study are  
171 plotted as a function of pressure in Figure 1c. Over the range of the lower mantle,  $Mg(C,Si)O_3$   
172 and  $MgCO_3 + Fe$  have negative mixing volumes.  $MgSiO_3 + Fe$  and  $Mg(C,Si)O_3 + Fe$  have  
173 positive mixing volumes.

174 To expand our analysis to any composition in the  $MgCO_3$ - $MgSiO_3$ -Fe ternary system, the  
175 mixing volume data is fit to the following power series multicomponent mixing model (Ganguly,  
176 2001; Wohl, 1946, 1953):

177 
$$\Delta V_{mix} = \sum_{i \neq j} X_i X_j (W_{ij}^G X_{ji} + W_{ji}^G X_{ij}) + \sum_{i \neq j, \neq k} X_i X_j X_k C_{ijk} \quad (4)$$

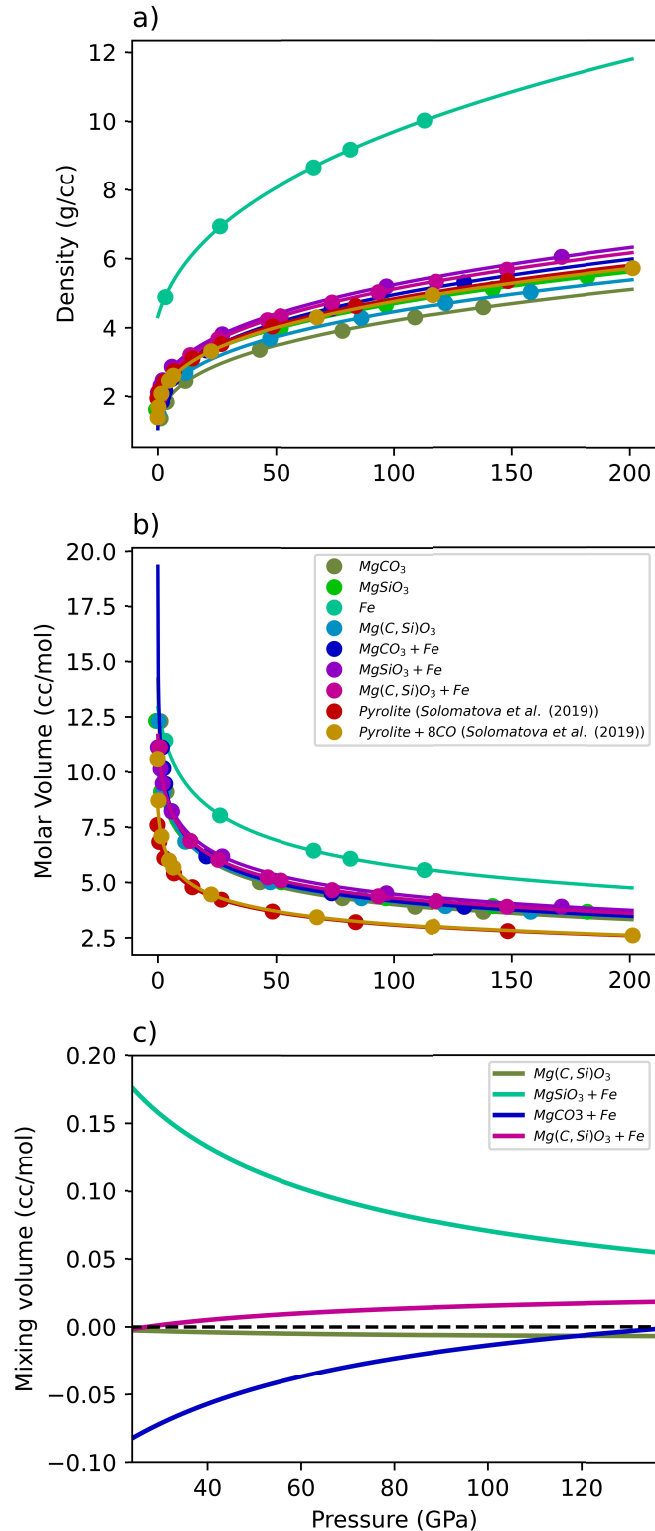


Figure 1: Density, molar volume, and mixing volume data for all simulated melt compositions are plotted as a function of pressure. a) Melt densities are fit to second or third-order Birch-Murnaghan equations of state. b) Molar volumes. Due to the non-stoichiometric nature of the ternary melt composition, we report volumes for all melt compositions per mole of atoms. c) Mixing volumes for all binary and ternary melt compositions over the pressure range of the Earth's lower mantle.

179 where  $\Delta V_{\text{mix}}$  is the mixing volume, the  $W^G$ 's are the binary interaction parameters, and  $C_{ijk}$  is the  
 180 ternary interaction term.  $X_i$ ,  $X_j$ , and  $X_k$  are the mole fractions of the  $i$ ,  $j$ , and  $k$  components, and  
 181  $X_{ji}$  and  $X_{ij}$  are the projected mole fractions of the  $i$  and  $j$  components in the binary join  $i$ - $j$ .  $X_{ij}$  is  
 182 given analytically by  $\frac{1}{2}(1+X_i-X_j)$ . Similar to our calculation of molar volumes, in this analysis,  
 183 we set the mole fractions by counting the number of atoms of each component, rather than the  
 184 number of formula units. Thus, each iron atom in the model is compared to an average atom of  
 185 either an  $\text{MgCO}_3$  or an  $\text{MgSiO}_3$  unit. For example, in our simulated ternary melt composition  
 186 ( $12\text{MgSiO}_3 + 12\text{MgCO}_3 + 13\text{Fe}$ ), the mole fractions are  $X_{\text{Fe}} = 0.1$ ,  $X_{\text{MgCO}_3} = 0.45$ , and  $X_{\text{MgSiO}_3} =$   
 187  $0.45$ , which are derived from the number of atoms of each component. Given the limited number  
 188 of simulations, in this model we assume that mixing along the binaries is symmetric, and thus  
 189  $W^G_{ij} = W^G_{ji}$ .

190 Figure 2a-c displays mixing volumes along the binary joins  $\text{MgCO}_3$ - $\text{MgSiO}_3$ ,  $\text{MgCO}_3$ -Fe,  
 191 and  $\text{MgSiO}_3$ -Fe at 24 GPa, 50 GPa, and 136 GPa, all at the temperature of 4,000 K, calculated  
 192 using the fit parameters reported in Table S9. Along the carbonate-silicate join, mixing volumes

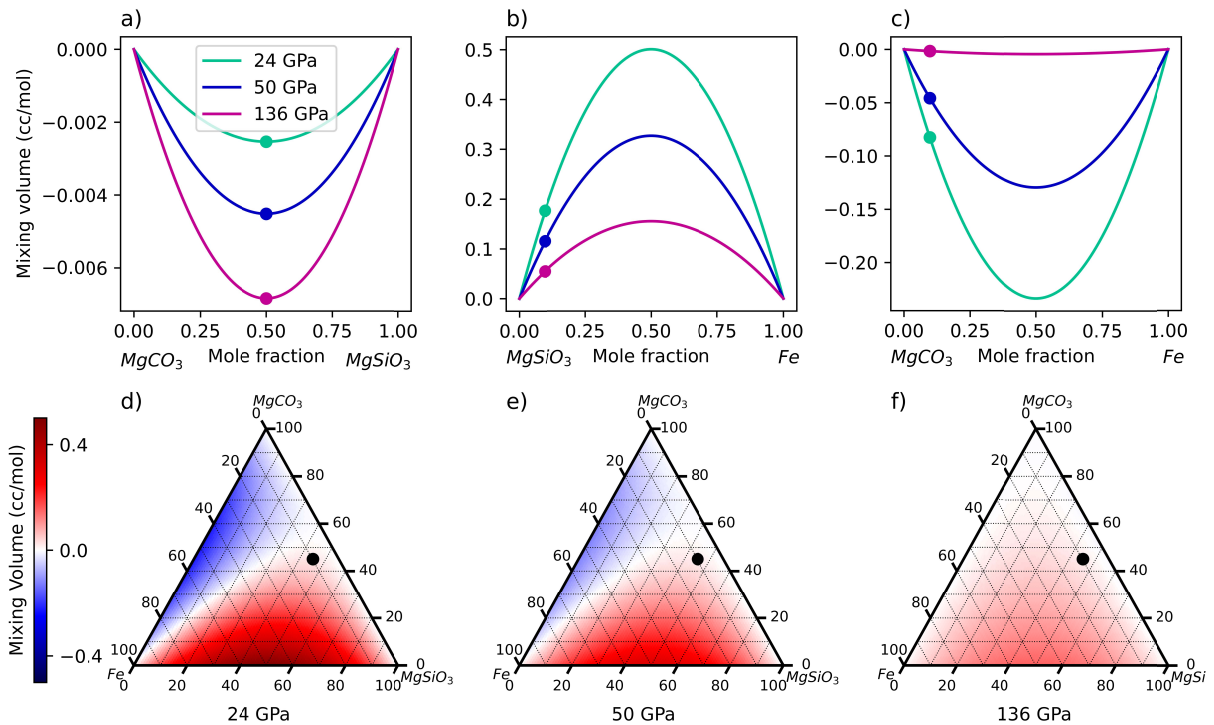


Figure 2: Mixing volumes for all binary and ternary melts are plotted as a function of melt composition. a-c) Mixing volumes for binary solutions of a)  $\text{MgCO}_3$  and  $\text{MgSiO}_3$ ; b)  $\text{MgSiO}_3$  and Fe; and c)  $\text{MgCO}_3$  and Fe at 24 GPa, 50 GPa, and 136 GPa. Simulated compositions are marked by data points, and lines are fits to the multicomponent mixing model. Both the  $\text{MgCO}_3$  and  $\text{MgSiO}_3$  binary and the  $\text{MgCO}_3$  and Fe binary have negative mixing volumes at lower mantle pressures, suggesting miscibility. The  $\text{MgSiO}_3$  and Fe binary has positive mixing volumes across all lower mantle pressures, suggesting immiscibility. d-f) Mixing volumes for ternary solutions of  $\text{MgCO}_3$ ,  $\text{MgSiO}_3$ , and Fe at d) 24 GPa; e) 50 GPa; and f) 136 GPa. Positive mixing volumes are shaded red and negative mixing volumes are shaded blue. The simulation composition used to fit the mixing model is marked by the data point, and always lies within the immiscible region of the plot.

193 are negative at all lower mantle conditions, and become more negative with increasing pressure,  
 194 suggesting continuous solubility. Along the silicate-metal join, mixing volumes are positive  
 195 across all lower mantle pressure conditions, and decrease with pressure. At pressures beyond  
 196 those of the Earth's mantle, we would expect silicate and metal melts to become miscible. Along  
 197 the carbonate-metal join, mixing volumes are always negative, but become less negative with  
 198 increasing pressure, suggesting potential immiscibility beyond the core-mantle boundary  
 199 pressure. Additionally, the magnitude of the mixing volumes represents the degree of interaction  
 200 between the melts. Generally, silicate-metal melts have the most interaction, followed by  
 201 carbonate-metal melts, and carbonate-silicate melts. Carbonate-silicate melt interaction terms are  
 202 very small, even at their most negative point at 136 GPa, indicating that this mixture is close to  
 203 ideal.

204 Figure 2d-f shows calculated mixing volumes for ternary compositions. At 24 GPa, melts  
 205 with greater than 50% carbonate have negative mixing volumes. For melts less than 50%  
 206 carbonate, mixing volumes are more negative with increasing iron percentage and more positive  
 207 with increasing silicate percentage. With increasing pressure, the negative mixing volume regime  
 208 shrinks and the positive mixing volume regime grows to cover more iron and carbonate-rich  
 209 parts of the ternary plot. By 136 GPa, only compositions that are greater than 70% carbonate and  
 210 compositions close to the carbonate-metal and carbonate-silicate binaries have negative mixing  
 211 volumes. Additionally, mixing volume magnitudes decrease with increasing pressure, indicating  
 212 that these melts tend to become more ideal with increasing pressure. This conclusion is  
 213 supported by the trends in the binary and ternary interaction parameters (Figure S3 and Table  
 214 S9). With increasing pressure, the interaction parameters trend towards 0, indicating that the  
 215 interaction between melt components becomes increasingly less important with depth.

### 216 3.4 Gibbs free energy of mixing

217 With the equations and approximations describing  $\Delta H_{\text{mix}}$ ,  $\Delta S_{\text{mix}}$ , and  $\Delta V_{\text{mix}}$ , we determine  
 218 how  $\Delta G_{\text{mix}}$  evolves along binary and ternary joins.  $\Delta G_{\text{mix}}$  is plotted along the carbonate-silicate,  
 219 carbonate-metal, and silicate-metal binaries in Figure 3a-c.  $\text{MgCO}_3$  and  $\text{MgSiO}_3$  melts  
 220 demonstrate limited miscibility at all lower mantle pressures, with a large miscibility gap. In the  
 221 immiscible region, two melt compositions coexist, and these compositions are determined by the  
 222 common tangent of the  $\Delta G_{\text{mix}}$  curves. These tangents are quasi-horizontal and have support  
 223 points that are very close to the minima of the free energy. The shared tangents of the curves are  
 224 plotted in Figure 4 and are at  $\sim 9$  and  $\sim 91$  mole percent  $\text{MgCO}_3$  at all pressures examined for the  
 225 carbonate-silicate binary.  $\Delta G_{\text{mix}}$  decreases with pressure, suggesting eventual closing of the  
 226 miscibility gap at higher pressures than those reached by Earth's mantle.  $\text{MgSiO}_3$  and Fe are  
 227 immiscible at all lower mantle pressures. The metallic character of the pure Fe melt makes it  
 228 incompatible with the insulating character of the molten silicate melts, and any iron that is  
 229 dissolved in the silicate is always incorporated as an ionic phase, FeO or  $\text{Fe}_2\text{O}_3$ . Similar to the  
 230  $\text{MgSiO}_3$  and  $\text{MgCO}_3$  binary, the  $\text{MgCO}_3$  and Fe binary also has a miscibility gap that begins to  
 231 close with increasing pressure. At 24 GPa, the two coexisting melt compositions are at 6 and 94  
 232 mole percent  $\text{MgCO}_3$ , but by 136 GPa, the two coexisting melt compositions are at 38 and 62  
 233  $\text{MgCO}_3$  mole percent (Figure 4).

234 The ternary diagrams (Figure 3d-f) show a range of miscibilities that expand with  
 235 increasing pressure. Miscible melt fields, outlined by solid gold lines, are estimated from  $\Delta G_{\text{mix}}$   
 236 values along each of the binaries. There are three miscibility fields, and each is located near an  
 237 endmember composition. As the carbonate-metal and the carbonate-silicate miscibility gaps  
 238 close with pressure, the miscibility fields grow to accommodate more mixing. In between the

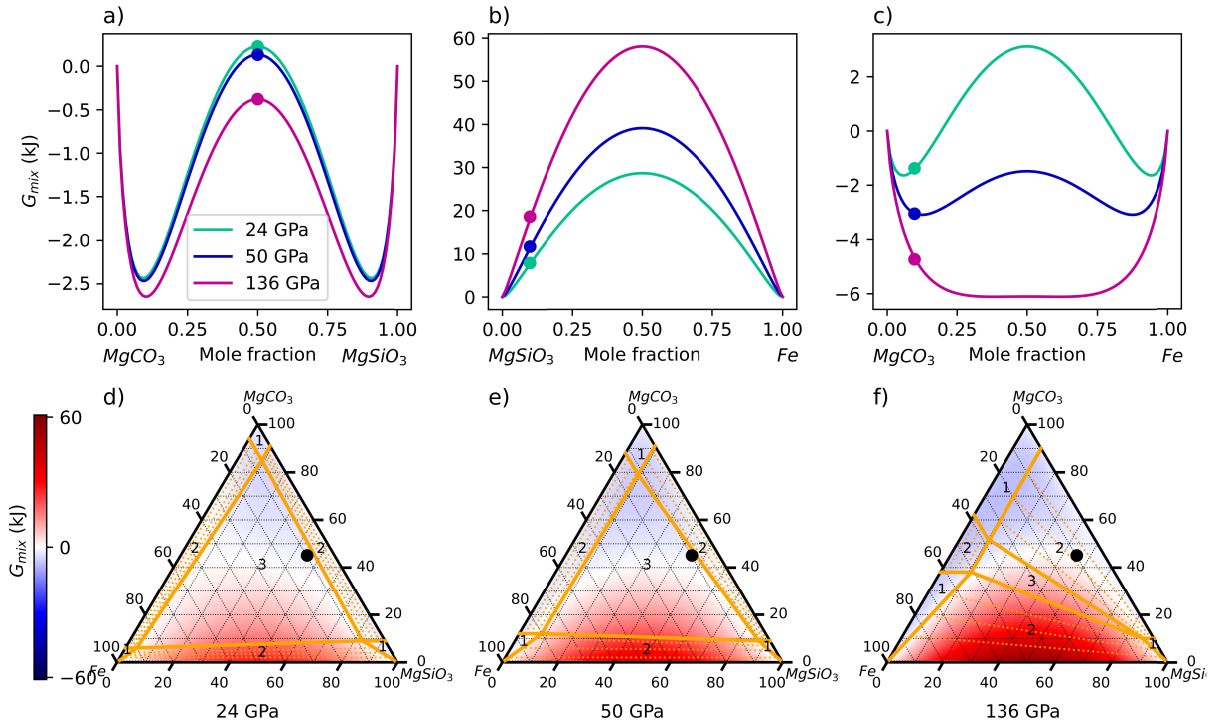


Figure 3:  $\Delta G_{\text{mix}}$  for all binary and ternary melts are plotted as a function of melt composition. a-c)  $\Delta G_{\text{mix}}$  for binary solutions of a)  $\text{MgCO}_3$  and  $\text{MgSiO}_3$ ; b)  $\text{MgSiO}_3$  and  $\text{Fe}$ ; and c)  $\text{MgCO}_3$  and  $\text{Fe}$  at 24 GPa, 50 GPa, and 136 GPa.  $\text{MgCO}_3$  and  $\text{MgSiO}_3$  have limited miscibility near the endmembers that increases with pressure, and  $\text{MgSiO}_3$  and  $\text{Fe}$  are immiscible at all pressures studied.  $\text{MgCO}_3$  and  $\text{Fe}$  have limited miscibility at 24 GPa, and the miscibility gap closes with increasing pressure. d-f)  $\Delta G_{\text{mix}}$  for ternary solutions of  $\text{MgCO}_3$ ,  $\text{MgSiO}_3$ , and  $\text{Fe}$  at d) 24 GPa; e) 50 GPa; and f) 136 GPa. Positive values of  $\Delta G_{\text{mix}}$  are shaded red and negative values are shaded blue. Solid gold lines outline miscible melt compositions, two coexisting melt regions, and three coexisting melt regions, labelled with a 1, 2, or a 3, respectively, and are estimated from the  $\Delta G_{\text{mix}}$  values on the binaries. Dashed gold lines are tie lines in the two melt regions. The ternary composition simulated for this study is labelled with a black dot.

239 miscibility fields are two-melt regions, and compositions that fall in these regions will exsolve  
 240 two immiscible melts. Dashed gold lines represent example tie lines in these regions. The central  
 241 triangle is the three-melt region, and compositions that fall in this region will exsolve three  
 242 immiscible melt compositions. With increasing pressure, the two-melt regions grow and the  
 243 three-melt region shrinks, indicating the overall increase in miscibility in this system at high  
 244 pressure. It is important to note that the chosen value for  $\Delta H_{\text{mix}}$  affects the miscibilities of the  
 245 melt mixtures. We estimate values for  $\Delta H_{\text{mix}}$  based on chemical speciation and literature  
 246 experiment, but without additional constraints there is some ambiguity in the selected value. The  
 247 blue regions of the plot indicate compositions with negative  $\Delta G_{\text{mix}}$  values, and thus, show a  
 248 possible range of miscible compositions that are available under smaller  $\Delta H_{\text{mix}}$  values.  
 249 Nonetheless, the results based on these reasonable estimates of  $\Delta H_{\text{mix}}$  illustrate the plausibility of  
 250 reduced immiscibility with increasing pressure in the carbonate-silicate-metal system, such that  
 251 an Fe-rich carbonate melt and a carbon-rich Fe melt would be expected to segregate from other  
 252 phases at the base of the mantle.

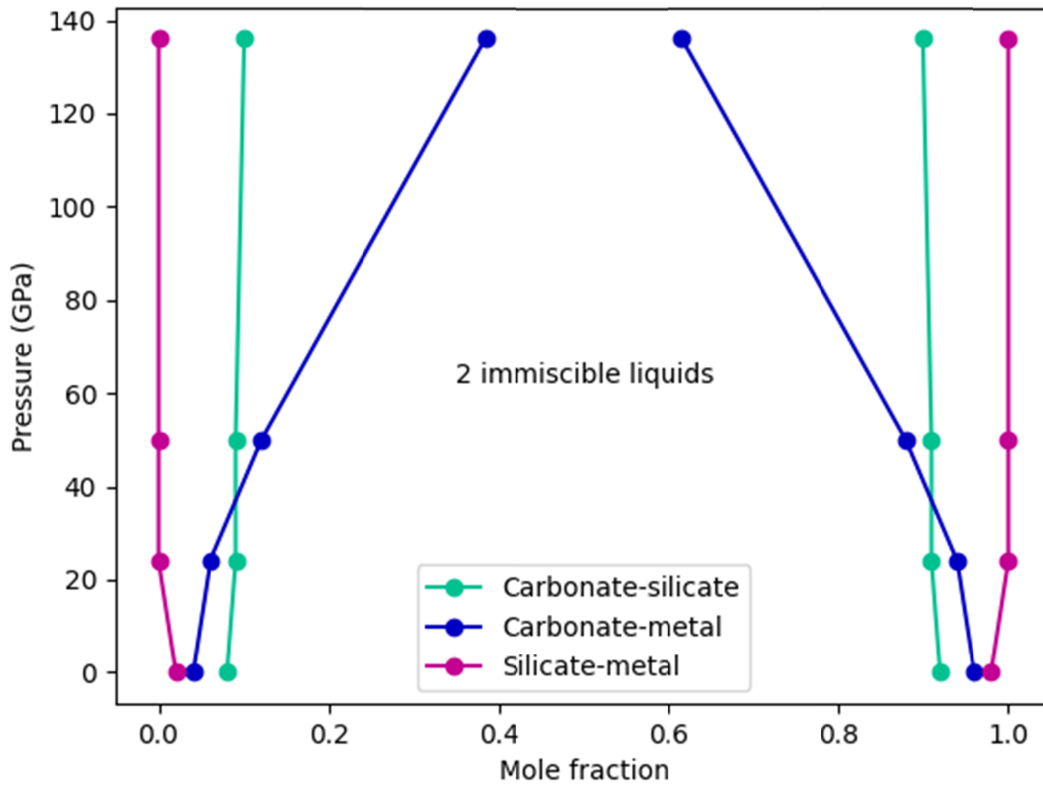


Figure 4: Phase diagram for binary melt mixtures with pressure. The central region inside each of the pairs of lines is the miscibility gap, where it is more energetically favorable to form two melt immiscible melt compositions. The miscibility gap closes with increasing pressure for carbonate-metal mixtures and widens for silicate-metal mixtures. Although the carbonate-silicate miscibility gap remains mostly constant at lower-mantle conditions, a decreasing  $\Delta G_{\text{mix}}$  suggests the eventual closing of the miscibility gap at higher pressures.

#### 253 4 Carbon-bearing clusters

254 As evidenced by Figure 3d-f, many carbonate-silicate-iron melt compositions are  
 255 immiscible at lower mantle conditions, even at the high-pressure conditions of the core-mantle  
 256 boundary. Although *ab initio* molecular dynamics cannot model phase separation because of size  
 257 effects, the clustering of species we observe in our simulations is suggestive of the process of  
 258 melt separation. In this section, we identify the species that segregate in an example ternary melt  
 259 mixture through speciation analysis, and we determine individual cluster densities to understand  
 260 how elements distribute through the lower mantle.

261 The example melt composition is the ternary melt composition simulated for this study  
 262 (10% Fe, 45%  $\text{MgCO}_3$ , 45%  $\text{MgSiO}_3$ ). A more complete speciation analysis of this melt  
 263 composition is reported in Davis et al. (2022). In general, large increases in C-Fe and C-C  
 264 bonding with pressure at the expense of C-O bonding are observed. No evidence of Fe-Si

265 bonding is found at any pressure. These tendencies are in good agreement with the predicted  
 266 miscibilities for binary solutions (Figure 3a-c). In the melt, large carbon-carbon clusters and, at  
 267 higher pressures, carbon-iron clusters form and have limited interaction with the silicate melt  
 268 network, indicating the types of carbon-bearing melt species we might expect to segregate from a  
 269 silicate melt. However, the extent of carbon-iron interaction is difficult to quantify. Carbon-iron  
 270 clusters often consist of iron atoms surrounding a polymerized carbon core, which could be  
 271 classified as either a diamond seed nucleus or an iron carbide cluster. Previous simulations  
 272 (Davis et al., 2022; Karki et al., 2020; Solomatova et al. 2019) show that we would expect  
 273 carbon to bond to O, Fe, C, and Si. For each carbon atom, we would expect 12% (13/108) of the  
 274 bonds to be C-Fe bonds, as there are 13 iron atoms from an available 108 coordinating anions for  
 275 carbon (12 silicon, 72 oxygen, 11 out of the 12 carbon, and 13 iron). Additionally, we anticipate  
 276 that 67% (72/108) of carbon bonds are to oxygen. Starting from these estimates based on the  
 277 statistical sampling, we classify the carbon-based clusters in the melt. Bond abundances greater  
 278 than the abundances predicted from statistical sampling indicate that there is a chemical

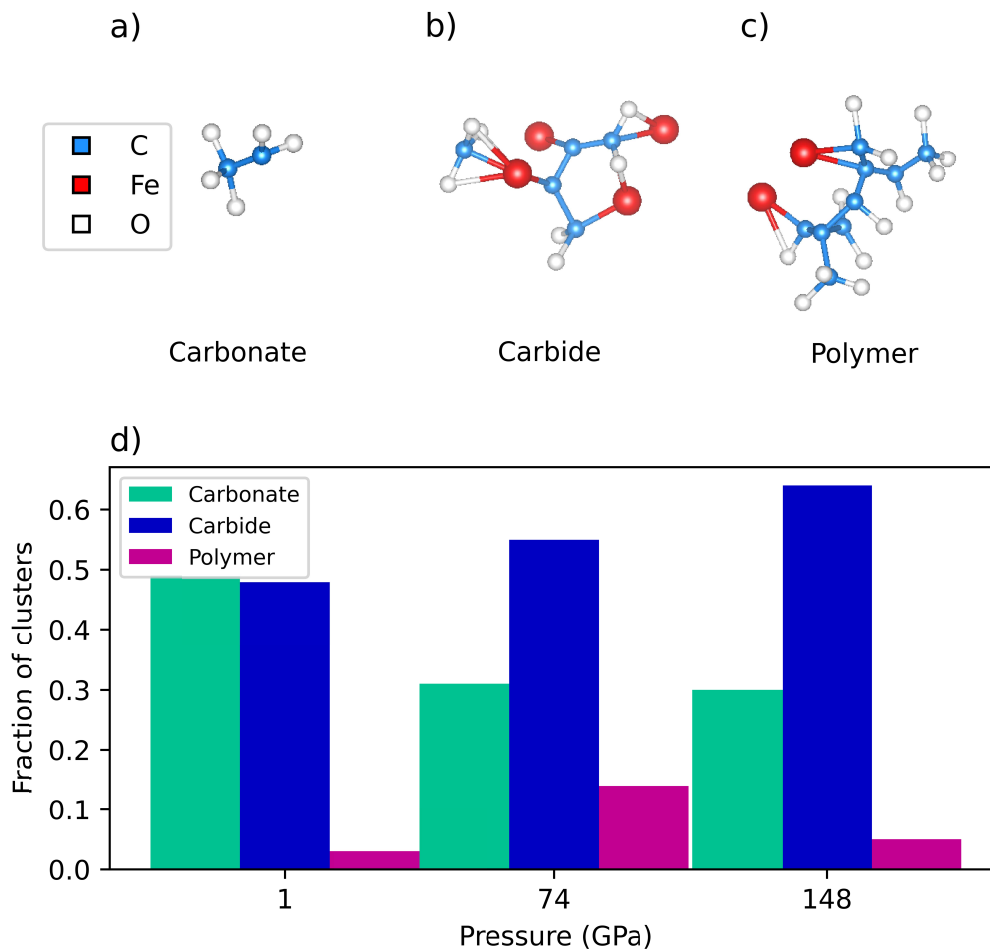


Figure 5: Examples of types of carbon-bearing clusters and their abundances. a-c) Examples of isolated carbon-iron-oxygen clusters classified as carbonate, carbide, and polymer from 74 GPa and 4,000 K. d) Abundances of carbonate, carbide, and polymer clusters with increasing pressure.

279 preference for the bonding element. In our cluster analysis, we classify carbon clusters with C-O  
 280 bond abundances greater than 67% as carbonates and carbon clusters with C-Fe bond  
 281 abundances greater than 12% as carbides. Clusters with less C-O and C-Fe abundances than  
 282 expected from statistical sampling are classified as carbon polymers. The abundances of the  
 283 different types of clusters at 1, 74, and 148 GPa are plotted in Figure 5d. At all three pressures,  
 284 clusters of each type are formed, but the relative abundances of the cluster types evolve with  
 285 pressure. Carbonates are the most abundant cluster type at 1 GPa and account for 49% of the  
 286 total clusters, but that number drops to 31% at 74 GPa and 30% at 148 GPa. Carbides almost  
 287 match the number of carbonate clusters at 1 GPa, at 48% of the total, and are the most abundant  
 288 cluster type at 74 and 148 GPa, at 55% and 64% of the total, respectively. Polymers are always  
 289 the least abundant cluster type. They increase in abundance from 3% to 14% from 1 to 74 GPa,  
 290 and then decrease in abundance to 5% at 148 GPa. In Davis et al. (2022), we noticed that the  
 291 majority of changes in C-O and C-C bond abundances occur in the first 25 GPa. Thus, we expect  
 292 diamond formation to peak around 25 GPa, and this expectation is reflected in the relative  
 293 increase in polymer formation between 1 and 74 GPa. Similarly, we expect carbonate cluster  
 294 abundance to decrease rapidly in the first 25 GPa, before plateauing, and this result is also  
 295 observed. Finally, the large and linearly increasing number of carbide clusters matches the  
 296 speciation results in both Davis et al. (2022) and Solomatova et al. (2019), which report linear  
 297 increases in C-Fe bond abundances with increasing pressure.

298 The composition and the volume of the carbon clusters determines their relative density  
 299 within the mantle. Using the Bader charge analysis algorithm (Henkelman et al, 2006; Sanville et  
 300 al., 2007; Tang et al., 2009; Yu & Trinkle, 2011), we calculate the volumes of individual atoms  
 301 within carbon clusters to determine cluster densities. Densities of example carbon clusters  
 302 isolated at 74 and 148 GPa are plotted in Figure 6. The selected clusters are grouped according to  
 303 their classification as a carbonate, carbide, or polymer. We directly compare the density of the  
 304 cluster to the calculated density of MgSiO<sub>3</sub> melt at the same conditions. Carbide clusters are  
 305 much denser than MgSiO<sub>3</sub> melt, and with enough time and aggregation, we expect these clusters  
 306 to segregate from the multicomponent melt and sink to the core. Similarly, polymers are slightly

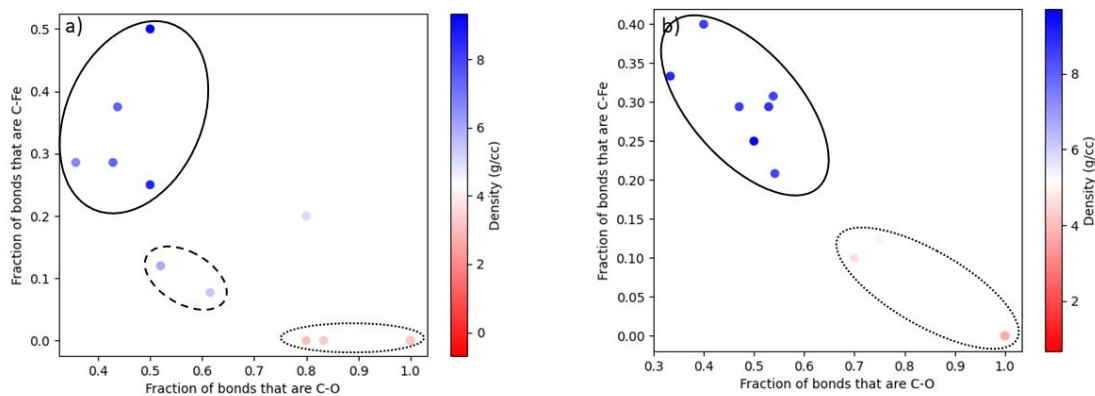


Figure 6: Carbon clusters identified from three separate snapshots at a) 74 GPa and b) 148 GPa and plotted by fraction of bonds that are C-O and fraction of bonds that are C-Fe. Points circled with a dotted line correspond to carbonates, with a solid line correspond to carbide, and with a dashed line correspond to polymers. Data points are colored by density of the cluster. Clusters denser than MgSiO<sub>3</sub> (blue) will sink and clusters less dense than MgSiO<sub>3</sub> (red) will float.

307 denser than  $\text{MgSiO}_3$  melt. Carbonate clusters are lighter than  $\text{MgSiO}_3$  melt, and we expect these  
 308 clusters to be buoyant within the mantle.

### 309 5 Implications

310 From the miscibility analysis, we find three miscible melt compositional fields:  
 311 carbonate-rich, silicate-rich, and iron-rich melts (Figure 3d-f). We consider the densities of these  
 312 melt compositions to determine their buoyancies in the lower mantle and to evaluate their  
 313 implications for carbon distribution and sequestration in the lower mantle and core. Densities of  
 314 liquids calculated from molecular dynamics methods have been shown to systematically deviate  
 315 from experimental values depending on the approximation used for the exchange correlation  
 316 functional (Zhang et al., 2013; Zhao et al., 2014). However, relative comparisons of density  
 317 between calculated melts are useful, provided the same approximations are made. As an  
 318 example, density differences from  $\text{MgSiO}_3$  melt at the core-mantle boundary are plotted in  
 319 Figure 7. Here, miscible melt compositions could be formed from a deep Earth carbonatite melt  
 320 interacting with iron melt at the core-mantle boundary. Compositions are shaded in red, white,  
 321 and blue to represent buoyant, neutrally buoyant, and dense compositions, respectively, as

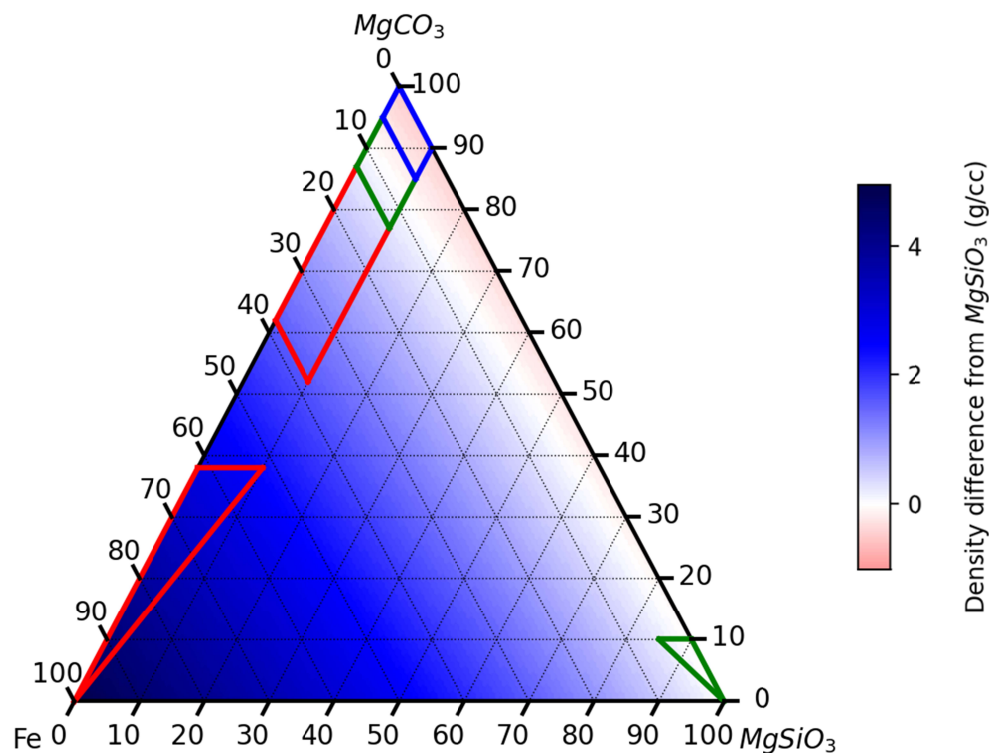


Figure 7: Densities of ternary melt compositions at 136 GPa compared to the density of  $\text{MgSiO}_3$  melt. Melts denser than  $\text{MgSiO}_3$  and less dense than pure Fe are colored blue, and would sink in the mantle. Melts less dense than  $\text{MgSiO}_3$  are colored red, and would float. Miscible melt compositions that would sink, float, and be neutrally buoyant are outlined with red, blue, and green lines, respectively.

322 compared to the density of  $\text{MgSiO}_3$  melt, which is used as a proxy for the lower mantle  
323 composition. Three groups of miscible compositions emerge. Compositions outlined in red are  
324 iron-rich and denser than  $\text{MgSiO}_3$ . We expect these compositions to sink into the outer core,  
325 dragging carbon and silicon out of the mantle and enriching the outer core with light elements  
326 over time. Compositions outlined in blue are carbonate-rich and buoyant. These compositions are  
327 anticipated to rise through the mantle and return carbon to shallower depths. Finally, the green  
328 compositions are neutrally buoyant and thus, gravitationally stable at the core-mantle boundary.  
329 These compositions could serve as possible contributors to ultra-low velocity zones (ULVZs).  
330 ULVZs have multiple proposed explanations, including FeSi formed through core-mantle  
331 reactions (Mergner et al., 2021), hydrous phases such as  $(\text{Al,Fe})\text{OOH}$  (Thompson et al., 2021),  
332 Fe-rich post perovskite (Garnero & McNamara, 2008), Fe-rich  $(\text{Mg,Fe})\text{O}$  (Solomatova et al.,  
333 2016; Wicks et al., 2010), and patches of partial melt (Williams & Garnero, 1996). Partial melt is  
334 a likely explanation for ULVZs due to the 3:1 ratio of S-to-P wave velocity reduction (Garnero  
335 & McNamara, 2008; Williams & Garnero, 1996). Therefore, buoyantly neutral melt  
336 compositions, such as the carbonate-silicate-metal melt compositions calculated in this study,  
337 could serve as one possible explanation and contributor to the ULVZs.

338 Within the immiscible melt compositions, carbon, carbon-iron, and carbon-oxygen  
339 clusters form (Figure 5). Given enough time and aggregation, we expect the carbon and carbon-  
340 iron clusters to exsolve from the melt, as has been previously suggested (Dasgupta &  
341 Hirschmann, 2010; Karki et al., 2020; Mysen et al., 2011; Stagno et al., 2013). In our example  
342 ternary melt composition, the majority of the clusters formed at 148 GPa are carbide (64%), and  
343 the propensity for carbon to bond with iron indicates carbon's high siderophilicity under these  
344 thermodynamic conditions. Carbide clusters are denser than the surrounding mantle (Figure 6).  
345 Thus, a significant amount of Earth's carbon contained in the lower mantle may bond with iron  
346 and sink to the core, matching previous *ab initio* predictions of carbon's fate under reduced  
347 conditions in the lower mantle (Karki et al., 2020; Rohrbach & Schmidt, 2011). This not only  
348 prevents carbon from being recycled back to the Earth's surface, but also changes the evolution  
349 of the core composition. An increasingly carbon-rich core composition would evolve to have  
350 density, sound velocities, and electrical and thermal conductivity more similar to the carbon-rich  
351 alloys  $\text{Fe}_3\text{C}$  and  $\text{Fe}_7\text{C}_3$  (Fiquet et al., 2009; Ghosh & Karki, 2017; Wood et al., 2013). Moreover,  
352 given the chemical preference of carbon to be bonded to iron, we propose that during core  
353 formation, iron droplets that segregate from the magma ocean and fall downwards would  
354 constitute strong attraction basins for carbon. In this way the magma ocean would be leached of  
355 its carbon. After the Moon-forming impact, metal and silicate melts would be well-mixed and  
356 siderophile elements like carbon would be segregated with iron into the core, supporting the idea  
357 that carbon is a candidate element to explain the density deficit in the core (Prescher et al., 2015;  
358 Solomatova et al., 2019).

359 In addition to carbide clusters, we observe the formation of carbon polymers in our  
360 simulated ternary melt composition, which could be precursors for diamonds. Our simulations  
361 reveal a possible mechanism for diamond formation, where carbon polymers exsolve from a  
362 silicate melt. Previously, this formation mechanism was observed in oxygen-deficient carbon-  
363 bearing silicate melts (Ghosh et al., 2017), and the addition of iron in our simulations may  
364 actually increase carbon polymerization (Belonoshko et al., 2015). Our previous speciation  
365 analysis of this melt composition (Davis et al., 2022) indicates that carbon-carbon bond  
366 formation reaches a peak around 25 GPa, beyond which it plateaus. C-Fe bonding, however,  
367 increases linearly and with increasing depth, the percentage of polymers decreases as carbide

368 clusters are preferentially formed. Thus, our analysis indicates a diamond formation zone around  
369 25 GPa. This depth in the Earth matches reports of diamonds with a deep Earth origin, which are  
370 returned from either the transition zone or the top of the lower mantle (Smith et al., 2016; Stachel  
371 et al., 2005). However, our cluster analysis (Figure 5) indicates that polymers are formed even at  
372 the core-mantle boundary, and if these polymers aggregate to form diamonds, these diamonds  
373 may be brought to the surface by deep mantle plumes. Diamonds with a lowermost mantle origin  
374 may be identified through compositional analysis of fluid inclusions. Diamonds containing  
375 silicate-poor metal-rich carbonate melt compositions that fall into the miscible melt regions  
376 indicated in Figure 3f would indicate a core-mantle boundary origin and would provide evidence  
377 for carbon-silicate-metal melt reactions in the lowermost mantle.

378 Finally, we examine the carbon distribution at pressure and temperature conditions of the  
379 core-mantle boundary to provide some insight for possible carbon distributions between core and  
380 mantle phases. We examine an equimolar composition (i.e. 1/3 Fe, 1/3 MgCO<sub>3</sub>, and 1/3  
381 MgSiO<sub>3</sub>), which falls into the three-melt region at the center of the ternary plot (Figure 3f). Of  
382 the three melts that exsolve from this composition, 31% is a carbonate-rich melt, 37% is an iron-  
383 rich melt, and 32% is a silicate-rich melt, where the melt compositions that exsolve are given by  
384 the corners of the miscible melt fields in Figure 3f. From mass balance calculations, we  
385 determine that for this case, 90% of the carbon is contained in outer-core compositions  
386 (carbonate-rich and iron-rich melts) and 10% is contained in a potential ULVZ composition  
387 (silicate-rich melt). In fact, carbon is distributed to varying degrees between outer-core and  
388 ULVZ-type compositions for the majority of compositions in this ternary system, and buoyant  
389 carbonate-rich melt phases only form when there is less than ~5% Fe in the system. At the core-  
390 mantle boundary where iron melt is abundant, we anticipate that carbon is preferentially stored in  
391 lower-mantle and core phases, indicating that the ultimate fate of Earth's carbon may be storage  
392 in the deep interior.

393

## 394 **6 Conclusions**

395 Carbonates are important compounds in the crust and upper mantle and may play a role  
396 in the lower mantle as well. Carbonate melts in the deep Earth may react with silicates and  
397 metals, especially at the core-mantle boundary where these phases are abundant. The chemical  
398 and physical properties of the melts that form from these reactions have important consequences  
399 for the distribution and storage of carbon in the deep Earth. Ab initio molecular dynamics  
400 simulations of carbonate-silicate-iron melt compositions allow for the examination of melt  
401 miscibilities, densities, and speciation. We find that carbonate-silicate and carbonate-iron melts  
402 have miscibility gaps that close with increasing pressure, and that carbonate-iron melts have the  
403 highest affinity for mixing. Silicate-iron melts are immiscible at all lower mantle pressures. By  
404 expanding our analysis to the ternary carbonate-silicate-iron system, we find that three miscible  
405 melt fields exist near each of the endmember compositions (Fe-rich, carbonate-rich, and silicate-  
406 rich melts). Iron-rich melts are dense and sink into the core, providing a mechanism to enrich the  
407 outer core in light elements such as carbon, oxygen, and silicon. Silicate-rich melts are neutrally  
408 buoyant and sit at the core-mantle boundary, providing one possible explanation for the existence  
409 of ultra-low velocity zones. Carbonate-rich melts, depending on their iron content, may sink into  
410 the core, remain at the core-mantle boundary, or rise through the mantle. Thus, depending on the  
411 composition that forms through reaction of carbonate, silicate, and iron phases, carbon may be  
412 stored in the deep Earth in core- or ULVZ-type compositions or may return to shallower depths.

413 The majority of melt compositions have densities that classify them as core- or ULVZ-type  
414 compositions, indicating that the fate of carbon may be to be stored in the Earth's deep interior.  
415 Finally, the speciation of carbonate-silicate-iron melts indicates that carbon polymers, iron  
416 carbides, and carbonate clusters are formed in the melt, and the relative proportions of these  
417 clusters at various pressures indicate carbon's changing affinity for the other elements. Iron  
418 carbides, which are favorably formed at higher pressure, indicate carbon's increasingly  
419 siderophile nature with depth. Carbon polymers, when aggregated, could form diamonds, and are  
420 abundant at transition zone pressures, indicating a propensity for diamond formation in and  
421 around the transition zone. The distribution of carbon throughout the Earth's interior is a  
422 complicated topic, affected by many thermodynamic variables, including pressure, temperature,  
423 composition, and oxygen fugacity. More experimental and computational studies of carbonate  
424 melts and their interactions with other phases at lower-mantle and especially core-mantle  
425 boundary conditions will help elucidate the role of carbon in the Earth's deep interior.

## 426 **Acknowledgments**

427 The authors declare no competing conflicts of interest. This research was supported with a  
428 Graduate Research Fellowship (DGE 1746045) to AHD, and with a National Science Foundation  
429 GROW grant to AHD, by the European Research Council (ERC) under the European Union's  
430 Horizon 2020 research and innovation program (Grant Agreement No. 681818-IMPACT to RC),  
431 and by the National Science Foundation with Grant EAR – 1651017 to AJC. We also  
432 acknowledge access to the PSMN supercomputer at ENS Lyon to perform all calculations.

433

## 434 **Open Research**

435 All simulation output presented in this manuscript is publicly available at  
436 <https://doi.org/10.5281/zenodo.7093216>

437

## 438 **References**

- 439 Bajgain, S. K., & Mookherjee, M. (2021), Carbon bearing aluminosilicate melt at high pressure.  
440 *Geochimica et Cosmochimica Acta*, 312, 106-123. doi: 10.1016/j.gca.2021.07.039
- 441 Belonoshko, A. B., Lukinoy, T., Rosengren, A., Bryk, T., & Litasov, K. D. (2015), Synthesis of  
442 heavy hydrocarbons at the core-mantle boundary. *Scientific Reports*, 5, 18382. doi:  
443 10.1038/srep18382
- 444 Blochl, P. E. (1994), Projector augmented-wave method. *Physical Review B*, 50, 17953-17979.  
445 doi: 10.1103/PhysRevB.50.17953

- 446 Caracas, R., Kobsch, A., Solomatova, N. V., Li, Z., Soubiran, F., & Hernandez, J.-A. (2021),  
447 Analyzing melts and fluids from ab initio molecular dynamics simulations with the UMD  
448 package. *Journal of Visualized Experiments*. doi: 10.3791/61534-v
- 449 Dasgupta, R., & Hirschmann, M. M. (2010), The deep carbon cycle and melting in Earth's  
450 interior. *Earth and Planetary Science Letters*, 298, 1-13. doi: 10.1016/j.epsl.2010.06.039
- 451 Dasgupta, R., & Walker, D. (2008), Carbon solubility in core melts in a shallow magma ocean  
452 environment and distribution of carbon between the Earth's core and the mantle. *Geochimica et*  
453 *Cosmochimica Acta*, 72, 4627-4641. doi: 10.1016/j.gca.2008.06.023
- 454 Davis, A. H., Solomatova, N. V., Campbell, A. J., & Caracas, R. (2022) The speciation and  
455 coordination of a deep Earth carbonate-silicate-metal melt. *Journal of Geophysical Research:*  
456 *Solid Earth*, 127. doi: 10.1029/2021JB023314
- 457 Dorfman, S. M., Badro, J., Nabiei, F., Prakapenka, V. B., Cantoni, M., & Gillet, P. (2018),  
458 Carbonate stability in the reduced lower mantle. *Earth and Planetary Science Letters*, 489, 84-  
459 91. doi: 10.1016/j.epsl.2018.02.035
- 460 Drewitt, J. W. E., Walter, M. J., Zhang, H., McMahon, S. C., Edwards, D., Heinen, B. J., et al.  
461 (2019), The fate of carbonate in oceanic crust subducted into Earth's lower mantle. *Earth and*  
462 *Planetary Science Letters*, 511, 213-222. doi: 10.1016/j.epsl.2019.01.041
- 463 Fichtner, C. E., Schmidt, M. W., Liebske, C., Bouvier, A.-S., & Baumgartner, L. P. (2021),  
464 Carbon partitioning between metal and silicate melts during Earth accretion. *Earth and*  
465 *Planetary Science Letters*, 554, 116659. doi: 10.1016/j.epsl.2020.116659
- 466 Fiquet, G., Badro, J., Gregoryanz, E., Fei, Y., & Occelli, F. (2009), Sound velocity in iron  
467 carbide (Fe<sub>3</sub>C) at high pressure: Implications for the carbon content of the Earth's inner core.  
468 *Physics of the Earth and Planetary Interiors*, 172, 125-129. doi: 10.1016/j.pepi.2008.05.016

- 469 Ganguly, J. (2001) in *Solid Solutions in Silicate and Oxide Systems* (ed C.A. Geiger) 37-70  
470 (European Mineralogical Union Notes in Mineralogy, Etvos University Press)
- 471 Garnero, E. J., & McNamara, A. K. (2008), Structure and dynamics of Earth's lower mantle.  
472 *Science*, 320, 626-628. doi: 10.1126/science.1148028
- 473 Ghosh, D. B., Bajgain, S. K., Mookherjee, M., & Karki, B. B. (2017), Carbon-bearing silicate  
474 melt at deep mantle conditions. *Scientific Reports*, 7, 848. doi: 10.1038/s41598-017-00918-x
- 475 Ghosh, D. B., & Karki, B. B. (2017), Transport properties of carbonated silicate melt at high  
476 pressure. *Science Advances*, 3. doi: 10.1126/sciadv.1701840
- 477 Ghosh, S., Ohtani, E., Litasov, K., Suzuki, A., & Sakamaki, T. (2007), Stability of carbonated  
478 magmas at the base of the Earth's upper mantle. *Geophysical Research Letters*, 34. doi:  
479 10.1029/2007GL031349
- 480 Henkelman, G., Arnaldsson, A., & Jónsson, H. (2006), A fast and robust algorithm for Bader  
481 decomposition of charge density. *Computational Materials Science*, 36, 354-360. doi:  
482 10.1016/j.commatsci.2005.04.010
- 483 Hoover, W. G. (1985), Canonical dynamics: Equilibrium phase-space distributions. *Physical*  
484 *Review A: General Physics*, 31, 1695-1697. doi: 10.1103/PhysRevA.31.1695
- 485 Javoy, M. (1997), The major volatile elements of the Earth: Their origin, behavior, and fate.  
486 *Geophysical Research Letters*, 24, 177-180. doi: 10.1029/96GL03931
- 487 Kamenetsky, V. S., & Yaxley, G. M. (2015), Carbonate-silicate liquid immiscibility in the  
488 mantle propels kimberlite magma ascent. *Geochimica et Cosmochimica Acta*, 158, 48-56. doi:  
489 10.1016/j.gca.2015.03.004

490 Karki, B. B., Ghosh, D. B., & Banjara, D. (2020), Mixed incorporation of carbon and hydrogen  
491 in silicate melts under varying pressure and redox conditions. *Earth and Planetary Science*  
492 *Letters*, 549. doi: 10.1016/j.epsl.2020.116520

493 Koura, N., Kohara, S., Takeuchi, K., Takahashi, S., Curtiss, L. A., Grimsditch, M., & Saboungi,  
494 M. (1996), Alkali carbonates: Raman spectroscopy, ab initio calculations, and structure. *Journal*  
495 *of Molecular Structure*, 382, 163-169. doi: 10.1016/0022-2860(96)09314-3

496 Korsakov, A. V., & Hermann, J. (2006), Silicate and carbonate melt inclusions associated with  
497 diamonds in deeply subducted carbonate rocks. *Earth and Planetary Science Letters*, 241, 104-  
498 118. doi: 10.1016/j.epsl.2005/10.037

499 Kresse, G., & Furthmuller, J. (1996), Efficient iterative schemes for ab initio total-energy  
500 calculations using a plane-wave basis set. *Physical Review B: Condensed Matter*, 54, 11169-  
501 11186. doi: 10.1103/physrevb.54.11169

502 Labrosse, S., Hernlund, J. W., & Coltice, N. (2007), A crystallizing dense magma ocean at the  
503 base of the Earth's mantle. *Nature*, 450, 866-869. doi: 10.1038/nature06355

504 Li, Z. Y., Li, J., Lange, R., Liu, J. C., & Mintzer, B. (2017), Determination of calcium carbonate  
505 and sodium carbonate melting curves up to Earth's transition zone pressures with implications  
506 for the deep carbon cycle. *Earth and Planetary Science Letters*, 457, 395-402. doi:  
507 10.1016/j.epsl.2016.10.027

508 Lv, M., Dorfman, S. M., Badro, J., Borensztajn, S., Greenberg, E., & Prakapenka, V. B. (2021),  
509 Reversal of carbonate-silicate cation exchange in cold slabs in Earth's lower mantle. *Nature*  
510 *Communications*, 12, 1712. doi: 10.1038/s41467-021-21761-9

511 McDonough, W. F., & Sun, S. S. (1995), The composition of the Earth. *Chemical Geology*, 120,  
512 223-253. doi: 10.1016/0009-2541(94)00140-4

513 Mergner, V., Kuppenko, I., Spiekermann, G., Petitgirard, S., Libon, L., Chariton, S., Krug, M., et  
514 al. (2021), Sound velocities in FeSi at lower mantle conditions and the origin of ultra-low  
515 velocity zones. *Geophysical Research Letters*, 48. doi: 10.1029/2020GL092257

516 Merlini, M., Crichton, W. A., Hanfland, M., Gemmi, M., Müller, H., Kuppenko, I., &  
517 Dubrovinsky, L. (2012), Structures of dolomite at ultrahigh pressure and their influence on the  
518 deep carbon cycle. *Proceedings of the National Academy of Sciences of the United States of*  
519 *America*, 109, 13509-13514. doi: 10.1073/pnas.1201336109

520 Mysen, B. O., Kumamoto, K., Cody, G. D., & Fogel, M. L. (2011), Solubility and solution  
521 mechanisms of C-O-H volatiles in silicate melt with variable redox conditions and melt  
522 composition at upper mantle temperatures and pressures. *Geochimica et Cosmochimica Acta*, 75,  
523 6183-6199. doi: 10.1016/j.gca.2011.07.035

524 Nosé, S. (1984), A unified formulation of the constant temperature molecular dynamics methods.  
525 *The Journal of Chemical Physics*, 81, 511-519. doi: 10.1063/1.447334

526 Oganov, A. R., Ono, S., Ma, Y., Glass, C. W., & Garcia, A. (2008), Novel high-pressure  
527 structures of MgCO<sub>3</sub>, CaCO<sub>3</sub>, and CO<sub>2</sub> and their role in Earth's lower mantle. *Earth and*  
528 *Planetary Science Letters*, 273, 38-47. doi: 10.1016/j.epsl.2008.06.005

529 Perdew, J. P., Burke, K., & Ernzerhof, M. (1996), Generalized gradient approximation made  
530 simple. *Physical Review Letters*, 77, 3865-3868. doi: 10.1103/PhysRevLett.77.3865

531 Plank, T., & Manning, C. E. (2019), Subducting carbon. *Nature*, 574, 343-352. doi:  
532 10.1038/s41586-019-1643-z

533 Prescher, C., Dubrovinsky, L., Bykova, E., Kuppenko, I., Glazyrin, K., Kantor, A., McCammon,  
534 C., et al. (2015), High Poisson's ratio of Earth's inner core explained by carbon alloying. *Nature*  
535 *Geosciences*, 8, 220-223. doi: 10.1038/ngeo2370

- 536 Rohrbach, A., & Schmidt, M. W. (2011), Redox freezing and melting in the Earth's deep mantle  
537 resulting from carbon-iron redox coupling. *Nature*, 472, 209-212. doi: 10.1038/nature09899
- 538 Sakamaki, T., Ohtani, E., Urakawa, S., Terasaki, H., & Katayama, Y. (2011), Density of  
539 carbonated peridotite magma at high pressure using an X-ray absorption method. *American*  
540 *Mineralogist*, 96, 553-557. doi: 10.2138/am.2011.3577
- 541 Sanville, E., Kenny, S. D., Smith, R., & Henkelman, G. (2007), Improved grid-based algorithm  
542 for Bader charge allocation. *Journal of Computational Chemistry*, 28, 899-908. doi:  
543 10.1002/jcc.20575
- 544 Smith, E. M., Shirey, S. B., Nestola, F., Bullock, E. S., Wang, J., Richardson, S. H., & Wang,  
545 W. (2016), Large gem diamonds from metallic liquid in Earth's deep mantle. *Science*, 354, 1403-  
546 1405. doi: 10.1126/science.aal1303
- 547 Solomatova, N. V., & Caracas, R. (2021), Buoyancy and structure of volatile-rich silicate melts.  
548 *Journal of Geophysical Research: Solid Earth*, 126. doi: 10.1029/2020JB021045
- 549 Solomatova, N., Caracas, R. and Cohen, R. (2020). Carbon Speciation and Solubility in Silicate  
550 Melts. In Carbon in Earth's Interior (eds C.E. Manning, J.-F. Lin and W.L. Mao). doi:  
551 10.1002/9781119508229.ch16
- 552 Solomatova, N. V., Caracas, R., & Manning, C. E. (2019), Carbon sequestration during core  
553 formation implied by complex carbon polymerization. *Nature Communications*, 10. doi:  
554 10.1038/s41467-019-08742-9
- 555 Solomatova, N. V., Jackson, J. M., Sturhahn, W., Wicks, J. K., Zhao, J., Toellner, T.S., Kalkan,  
556 B., et al. (2016), Equation of state and spin crossover of (Mg,Fe)O at high pressure, with  
557 implications for explaining topographic relief at the core-mantle boundary. *American*  
558 *Mineralogist*, 101, 1084-1093. doi: 10.2138/am-2016-5510

- 559 Stachel, T., Brey, G. P., & Harris, J. W. (2005), Inclusions in sublithospheric diamonds:  
560 Glimpses of deep Earth. *Elements*, 1, 73-78. doi: 10.2113/gselements.1.2.73
- 561 Stagno, V., Ojwang, D. O., McCammon, C. A., & Frost, D. J. (2013), The oxidation state of the  
562 mantle and the extraction of carbon from Earth's interior. *Nature*, 493, 84-88. doi:  
563 10.1038/nature11679
- 564 Tang, W., Sanville, E., & Henkelman, G. (2009), A grid-based Bader analysis algorithm without  
565 lattice bias. *Journal of Physics: Condensed Matter*, 21, 084204. doi: 10.1088/0953-  
566 8984/21/8/084204
- 567 Thompson, E. C., Campbell, A. J., & Tsuchiya, J. (2021), Elastic properties of the pyrite-type  
568 FeOOH-AlOOH system from first-principles calculations. *Geochemistry, Geophysics,*  
569 *Geosystems*, 22. doi: 10.1029/2021GC009703
- 570 Wicks, J. K., Jackson, J. M., & Sturhahn, W. (2010), Very low sound velocities in iron-rich  
571 (Mg,Fe)O: Implications for the core-mantle boundary region. *Geophysical Research Letters*, 37,  
572 L15304. doi: 10.1029/2010GL043689
- 573 Williams, Q., & Garnero, E. J. (1996), Seismic evidence for partial melt at the base of Earth's  
574 mantle. *Science*, 273, 1528-1530. doi: 10.1126/science.273.5281.1528
- 575 Wohl, K. (1946), Thermodynamic evaluation of binary and ternary liquid systems. *Transactions*  
576 *of the American Institute of Chemical Engineers*, 42, 215-249.
- 577 Wohl, K. (1953), Thermodynamic evaluation of binary and ternary liquid systems. *Chemical*  
578 *Engineering Progress*, 49, 218-221. doi:
- 579 Wood, B.J., Li, J., & Shahar, A., (2013), Carbon in the core: Its influence on the properties of  
580 core and mantle. *Reviews in Mineralogy and Geochemistry*, 75, 231-250. doi:  
581 10.2138/rmg.2013/75.8

- 582 Xu, M., Jing, Z., Bajgain, S. K., Mookherjee, M., Van Orman, J. A., Yu, T., & Wang, Y. (2020),  
583 High-pressure elastic properties of dolomite melt supporting carbonate-induced melting in deep  
584 upper mantle. *Proceedings of the National Academy of Sciences of the United States of America*,  
585 *117*, 18285-18291. doi: 10.1073/pnas.2004347117
- 586 Yu, M., & Trinkle, D. R. (2011), Accurate and efficient algorithm for Bader charge integration.  
587 *The Journal of Chemical Physics*, *134*, 064111. doi: 10.1063/1.3553716
- 588 Zhang, Y., & Yin, Q. Z. (2012), Carbon and other light element contents in the Earth's core  
589 based on first-principles molecular dynamics. *Proceedings of the National Academy of Sciences*  
590 *of the United States of America*, *109*, 19579-19583. doi: 10.1073/pnas.1203826109
- 591 Zhang, Z., Stixrude, L., & Brodholt, J. (2013), Elastic properties of MgSiO<sub>3</sub>-perovskite under  
592 lower mantle conditions and the composition of the deep Earth. *Earth and Planetary Science*  
593 *Letters*, *379*, 1-12. doi: 10.1016/j.epsl.2013.07.034
- 594 Zhao, G., Mu, H. F., Tan, X. M., Wang, D. H., & Yang, C. L. (2014), Structural and dynamical  
595 properties of MgSiO<sub>3</sub> melt over the pressure range 200-500 GPa: Ab initio molecular dynamics.  
596 *Journal of Non-Crystalline Solids*, *385*, 169-174. doi: 10.1016/j.jnoncrysol.2013.11.024